

Application of ultrasound artificial intelligence in the differential diagnosis between benign and malignant breast lesions of BI-RADS 4A

Sihua Niu

Peking University People's Hospital

Jianhua Huang

Harbin Institute of Technology

Jia Li

Southeast University Zhongda Hospital

Xueling Liu

The First Affiliated Hospital of Guangxi University of Chinese Medicine

Dan Wang

The first Affiliated Hospital of Guangxi University of Chinese Medicine

Ruifang Zhang

Zhengzhou University First Affiliated Hospital

Yingyan Wang

Southeast University Zhongda Hospital

Huiming Shen

Southeast University Zhongda Hospital

Min Qi

Southeast University Zhongda Hospital

Yi Xiao

Harbin Institute of Technology

Mengyao Guan

Harbin Institute of Technology

Haiyan Liu

Zhengzhou University First Affiliated Hospital

Diancheng Li

Peking University People's Hospital

Feifei Liu

Peking University People's Hospital

Xiuming Wang

Peking University People's Hospital

Yu Xiong

Peking University People's Hospital

Siqi Gao

Peking University People's Hospital

Xue Wang

Peking University People's Hospital

Jiaan Zhu (✉ zhujiiaan@pkupk.edu.cn)

Peking University People's Hospital <https://orcid.org/0000-0001-8700-639X>

Research article

Keywords: Artificial intelligence, Breast, BI-RADS 4A, Differential diagnosis

Posted Date: September 16th, 2020

DOI: <https://doi.org/10.21203/rs.3.rs-40074/v3>

License:  This work is licensed under a Creative Commons Attribution 4.0 International License.

[Read Full License](#)

Version of Record: A version of this preprint was published on October 2nd, 2020. See the published version at <https://doi.org/10.1186/s12885-020-07413-z>.

1 Application of ultrasound artificial intelligence in the differential diagnosis
2 between benign and malignant breast lesions of BI-RADS 4A

3

4 Sihua Niu¹, Jianhua Huang², Jia Li³, Xueling Liu⁴, Dan Wang⁴, Ruifang Zhang⁵,
5 Yingyan Wang³, Huiming Shen³, Min Qi³, Yi Xiao², Mengyao Guan², Haiyan Liu⁵,
6 Diancheng Li¹, Feifei Liu¹, Xiuming Wang¹, Yu Xiong¹, Siqu Gao¹, Xue Wang¹, Jiaan
7 Zhu^{1#}

8

9 1. Department of Ultrasound, Peking University People's Hospital, Beijing, 100044,
10 China

11 2. School of Computer Science and Technology, Harbin Institute of Technology,
12 Harbin, Heilongjiang Province, 150001

13 3. Department of Ultrasound, Southeast University Zhongda Hospital, Nanjing,
14 Jiangsu Province, 210009

15 4. Department of Ultrasound, The First Affiliated Hospital of Guangxi University of
16 Chinese Medicine, Nanning, Guangxi Zhuang autonomous region, 530023

17 5. Department of Ultrasound, Zhengzhou University First Affiliated Hospital,
18 Zhengzhou, Henan Province, 450052

19

20 # Corresponding author: Jiaan Zhu canzhujia@126.com

21

22

23 **Abstract**

24 **Background:** The classification of Breast Imaging Reporting and Data System 4A
25 (BI-RADS 4A) lesions is mostly based on the personal experience of doctors and lacks
26 specific and clear classification standards. The development of artificial intelligence
27 (AI) provides a new method for BI-RADS categorisation. We analysed the ultrasonic
28 morphological and texture characteristics of BI-RADS 4A benign and malignant
29 lesions using AI, and these ultrasonic characteristics of BI-RADS 4A benign and
30 malignant lesions were compared to examine the value of AI in the differential
31 diagnosis of BI-RADS 4A benign and malignant lesions.

32 **Methods:** A total of 206 lesions of BI-RADS 4A examined using ultrasonography
33 were analysed retrospectively, including 174 benign lesions and 32 malignant lesions.
34 All of the lesions were contoured manually, and the ultrasonic morphological and
35 texture features of the lesions, such as circularity, height-to-width ratio, margin
36 spicules, margin coarseness, margin indistinctness, margin lobulation, energy, entropy,
37 grey mean, internal calcification and angle between the long axis of the lesion and skin,
38 were calculated using grey level gradient co-occurrence matrix analysis. Differences
39 between benign and malignant lesions of BI-RADS 4A were analysed.

40 **Results:** Significant differences in margin lobulation, entropy, internal calcification
41 and ALS were noted between the benign group and malignant group ($P=0.013$, 0.045 ,
42 0.045 , and 0.002 , respectively). The malignant group had more margin lobulations and
43 lower entropy compared with the benign group, and the benign group had more internal
44 calcifications and a greater angle between the long axis of the lesion and skin compared

45 with the malignant group. No significant differences in circularity, height-to-width
46 ratio, margin spicules, margin coarseness, margin indistinctness, energy, and grey
47 mean were noted between benign and malignant lesions.

48 **Conclusions:** Compared with the naked eye, AI can reveal more subtle differences
49 between benign and malignant BI-RADS 4A lesions. These results remind us carefully
50 observation of the margin and the internal echo is of great significance. With the help of
51 morphological and texture information provided by AI, doctors can make a more
52 accurate judgment on such atypical benign and malignant lesions.

53 **Keywords:** Artificial intelligence; Breast; BI-RADS 4A; Differential diagnosis

54

55 **Background**

56 The Breast Imaging Reporting and Data System (BI-RADS) facilitates
57 communications among radiologists, clinicians and patients via the use of standardised
58 descriptions of lesions and reports, which greatly promotes the application of breast
59 imaging in clinical practice. BI-RADS 4A lesions exhibit a low suspicion for
60 malignancy of 2-10% and primarily include some atypical benign and malignant
61 lesions [1]. The 2013 BI-RADS does not provide specific guidance for the sub-category
62 of BI-RADS 4 lesions. The classification of these lesions is mostly based on the
63 personal experience of doctors and lacks specific and clear classification standards. The
64 large ultrasonic feature span of atypical benign and malignant lesions creates the
65 possibility of misclassification in the BI-RADS 4A category.

66 The development of artificial intelligence (AI) provides a new method for
67 BI-RADS classification [2]. AI can calculate the morphological and texture features of
68 breast lesions in ultrasonic images and overcome the shortcomings of human visual
69 observation [3,4,5]. At present, the application of AI in BI-RADS classification mainly
70 focuses on the feasibility and accuracy of different AI procedures [6-10]. AI can
71 achieve a classification level similar to that of radiologists [6,9]. Through the
72 quantitative study of BI-RADS classification features, some studies have reported
73 morphological and textural features that are different between benign and malignant
74 lesions. The shape, margin, internal echo and posterior echo of tumour can be used as
75 the differential diagnosis points of benign and malignant lesions [6, 8, 11]. Some other
76 studies focus on the differences in morphological and textural features among different
77 BI-RADS categories or specific diseases, for example, triple-negative breast cancer and
78 fibroadenoma [6, 12-14]. Studies investigating the application of AI between BI-RADS
79 4A benign and malignant lesions are limited. The present study analysed the ultrasonic
80 morphological and texture characteristics of BI-RADS 4A benign and malignant
81 lesions using AI and aimed at examining the value of AI in the differential diagnosis of
82 BI-RADS 4A benign and malignant lesions.

83 **Methods**

84 All of the patients were from Peking University People's Hospital, Southeast
85 University Zhongda Hospital, the First Affiliated Hospital of Guangxi University of
86 Chinese Medicine and Zhengzhou University First Affiliated Hospital. The ethics
87 committees of the four hospitals approved this study. Written informed consents were

88 obtained from all participants. All the doctors participated in the ultrasonic
89 examinations. All lesions diagnosed as BI-RADS 4A before surgery from January 2019
90 to December 2019 were collected and analysed retrospectively. According to the ACR
91 BI-RADS® Atlas Fifth Edition, two doctors (SHN and XW) with more than 10 years'
92 experience in breast ultrasound diagnosis who were blind to the pathological results
93 evaluated the suspicion for malignancy of all the lesions separately, and lesions with
94 low suspicion for malignancy (2-10%) were classified as BI-RADS 4A.

95 The inclusion criteria were as follows: (1) lesions were classified as BI-RADS 4A
96 by the two doctors finally; (2) the lesions were clear in grey-scale images without
97 measurement labels and the sample window of colour Doppler; (3) lesions should be
98 displayed within a high-frequency probe, and those less than 5 cm were included
99 according to the width of high-frequency probes; (4) all lesions were surgically
100 resected and pathologically diagnosed. The following exclusion criteria were employed:
101 (1) lesions were displayed in colour Doppler ultrasound images; (2) measurement
102 labels were present in grey scale images; (3) the transverse diameter of lesions
103 exceeded the width of probes.

104 Among them, 194 lesions were both classified as BI-RADS 4A by the two doctors.
105 Twelve cases with inconsistent classification were determined as BI-RADS 4A after
106 discussion by the two doctors. Finally, 206 lesions were enrolled in our study.

107 The ultrasound instruments used in this study included Aixplorer (Supersonic
108 Imagine, Aix-en-Provence, France), Aplio 500 (Toshiba Medical Systems, Otawara,
109 Tochigi, Japan), and Logic E9 (GE Healthcare, Milwaukee, WI, USA) instruments.

110 The AI software used in this research was the breast ultrasound intelligent
111 diagnosis system developed by the Harbin Institute of Technology. All lesions were
112 manually contoured, and the region of interest (ROI) was calculated using grey gradient
113 co-occurrence matrix analysis to obtain the morphological and texture features.

114 The morphological features included circularity, height-to-width ratio, margin
115 spicules, margin coarseness, margin indistinctness, margin lobulation, internal
116 calcification and angle between the long axis of the lesion and skin (ALS). The
117 principles of these features were as follows:

118 (1) Circularity

119 Circularity (Cir) described the similarity between tumours and circle, and it was
120 calculated according to the following formula [1]:

$$Cir = \frac{C^2}{S} \quad [1]$$

121 C was the number of pixels in the tumour boundary, which was equivalent to the
122 perimeter of the tumour, and S was the number of pixels contained in the tumour area,
123 which could be regarded as the area of the tumour.

124 (2) Height-to-width ratio

125 The height-to-width ratio (HWR) calculated the circumscribed rectangle of the
126 tumour boundary first to obtain the height and width of the circumscribed rectangle and
127 then calculated the ratio of the two using the formula [2]:

$$HWR = \frac{H}{W} \quad [2]$$

128 (3) Margin spicules

129 The coordinates of the margin pixels (x_i, y_i) were set to coordinates in polar
 130 coordinates (r_i, θ_i) according to centroid coordinates (x_0, y_0) . Then, the coordinates were
 131 rearranged clockwise (or anticlockwise). Then, Fourier transformation was performed,
 132 and the frequency spectrum data were obtained. The number of margin spicules (MS)
 133 was calculated according to the following formula [3]:

$$MS = \frac{\sum_{\omega=0}^{\frac{\pi}{4}} R(\omega)}{\sum_{\omega=\frac{\pi}{4}}^{\pi} R(\omega)} \quad [3]$$

134 (4) Margin coarseness

135 Margin coarseness (MC) reflected the degree of coarseness of tumour margin,
 136 which was given by equation [4]:

$$MC = \frac{1}{N} \sum_{i=1}^N |d_i - d_{i+1}| \quad [4]$$

137 Here, d_i reflected the distance (in pixel units) of the i_{th} pixel on the boundary to the
 138 centroid coordinates of the tumour, and d_i was arranged and calculated according to the
 139 clockwise (or anticlockwise) order of the corresponding pixels on the boundary.

140 (5) Margin indistinctness

141 The coarse boundary of tumour in the original grey-scale ultrasound image was
 142 calculated using a rough segmented ROI image, and tissue surrounding the tumour was
 143 regarded as the boundary area. The pixel gradient in horizontal and vertical directions
 144 of the boundary area was calculated using the Sobel operator, and the margin
 145 indistinctness (MI) was calculated according to the following formula [5]:

$$MI = \sum_{i=1}^n \sum_{j=1}^m \sqrt{d_x(i, j)^2 + d_y(i, j)^2} \quad [5]$$

146 M and n represented the size of the image, and d_x and d_y represented the gradient in
147 the horizontal and vertical directions of the pixel at the tumour boundary, respectively.

148 (6) Margin lobulation

149 The coordinates of the margin pixels (x_i, y_i) were converted to coordinates in polar
150 coordinates (r_i, θ_i) according to centroid coordinates (x_0, y_0) . Here, θ_i was converted to
151 the polar coordinate sequence $(r_1, \theta_1), (r_2, \theta_2), (r_3, \theta_3), \dots (r_i, \theta_i) \dots (r_n, \theta_n)$ according to
152 the clockwise (or anticlockwise) order. The median filter of frame size 21 was used to
153 reduce the influence of image noise, and the sequence was fitted with a polynomial of
154 degree 20. The sum of the maximum and minimum points was obtained as the value of
155 margin lobulation (ML) listed in the formula [6].

$$ML = \text{sum}(f_{\text{极大}}) + \text{sum}(f_{\text{极小}}) \quad [6]$$

156 (7) Internal calcification

157 First, the irrelevant region outside the tumour was set as zero pixels according to
158 the coarse segmentation results, and the interior region of the tumour was binarized
159 according to the mean grey value and the maximum value. Then, the binary image was
160 processed by morphology expansion and corrosion to remove the interference pixels;
161 finally, the number of connected regions of the white spots in the binary image was the
162 number of internal calcifications in the image.

163 (8) ALS

164 ALS θ described the angle between the tumour area and the horizontal direction.
165 The ellipse fitting algorithm was used to fit the tumour boundary of ROI image, and the
166 fitted ellipse centre, long axis, short axis, the positive angles of long axis and X axis

167 were obtained. The following transformation was performed according to the formula
 168 [7]:

$$\left\{ \begin{array}{l} \theta, 0 \leq \theta \leq \frac{\pi}{2} \\ \pi - \theta, \frac{\pi}{2} \leq \theta \leq \pi \\ \theta - \pi, \pi \leq \theta \leq \frac{3\pi}{2} \\ 2\pi - \theta, \frac{3\pi}{2} \leq \theta \leq 2\pi \end{array} \right. \quad [7]$$

169 Texture features included energy, entropy and grey mean. The number of pixels
 170 with a grey level of i and gradient of j in the gradient image simultaneously was the
 171 value of $H(i, j)$. Here, $H(i, j)$ was normalised to obtain $P(i, j)$, and $P(i, j)$ was used to
 172 calculate these texture features. The calculations of energy, entropy and grey mean
 173 were according to the formulas [8] [9] [10], respectively:

174 (1) Energy (E)

$$E = \sum_{i=1}^{L_s} \sum_{j=1}^{L_g} P(i, j)^2 \quad [8]$$

175 (2) Entropy (Ent)

$$Ent = - \sum_{i=1}^{L_s} \left(\sum_{j=1}^{L_g} P(i, j) * \log \sum_{j=1}^{L_g} P(i, j) \right) \quad [9]$$

176 (3) Grey mean (GM)

$$GM = \sum_{i=1}^{L_s} i * \sum_{j=1}^{L_g} P(i, j) \quad [10]$$

177

178 **Statistical analysis**

179 The SPSS version 17.0 software package for Windows (IBM Corporation,
 180 Armonk, NY, USA) was used for data analyses. Descriptive statistics and frequencies

181 were provided for circularity, height-to-width ratio, margin spicules, margin coarseness,
 182 margin indistinctness, margin lobulation, energy, entropy, grey mean, internal
 183 calcification and ALS, which were all normal distribution. Means \pm standard deviation
 184 were used to describe these features. Two independent samples t-test was used to
 185 compare two means in the sample. $P < 0.05$ indicated a statistically significant
 186 difference.

187 **Results**

188 All of the 206 patients were female. All of the lesions were isolated. A total of 174
 189 cases were benign. The median patient age was 39 years (range: 26-57 years), and the
 190 median lesion size was 1.6 cm (range: 0.6-4.2 cm). Thirty two cases were malignant.
 191 The median patient age was 43 years (range: 32-63 years), and the median lesion size
 192 was 1.3 cm (range: 0.8-2.5 cm). The pathological types of benign lesions and malignant
 193 lesions were presented in Table 1.

194 Table 1 Pathological types of benign lesions and malignant lesions

	Pathological types	n	%
Benign lesions	Adenosis	67	38.5
	Benign phyllodes tumour	6	3.4
	Fibroadenoma	68	39.1
	Inflammation	8	4.6
	Intraductal papilloma	20	11.5
	Complex cyst	5	2.9
Malignant lesions	Intraductal carcinoma in situ	12	37.5
	Intraductal papillary carcinoma	2	6.3

Invasive ductal carcinoma

18

56.2

195 Data for the circularity, height-to-width ratio, margin spicules, margin coarseness,
196 margin indistinctness, margin lobulation, energy, entropy, mean of grey level, internal
197 calcification and ALS were presented in Table 2.

198 Table 2 Morphological and texture characteristics of benign and malignant groups

	Benign group	Malignant group	<i>P</i>
Circularity	23.62±6.85	27.53±13.45	0.240
Height-to-width ratio	0.59±0.27	0.69±0.16	0.343
Margin spicules	14.60±9.40	14.67±11.01	0.960
Margin coarseness (pixel)	2.78±2.52	3.43±3.00	0.420
Margin indistinctness (E6)	2.19±9.03	2.23±7.36	0.610
Margin lobulation	7.68±2.55	9.58±3.40	0.013
Energy	0.03±0.02	0.04±0.03	0.271
Entropy	2.34±0.13	2.23±0.20	0.045
Grey mean	0.52±0.17	0.49±0.28	0.957
Internal calcification	3.78±4.29	2.53±2.05	0.045
ALS (degree)	13.58±18.42	6.32±5.65	0.002

199 Statistically significant differences in margin lobulation, entropy, internal
200 calcification and ALS were noted between the benign and malignant groups. The
201 malignant group exhibited increased margin lobulation (Fig. 1) and lower entropy
202 compared with the benign group, and the benign group had more internal calcifications
203 and increased ALS compared with the malignant group (Fig. 2). No significant
204 differences in circularity, height-to-width ratio, margin spicules, margin coarseness,

205 margin indistinctness, energy, and grey mean were noted between the benign and
206 malignant groups.

207

208 **Discussion**

209 AI exhibits high accuracy in the diagnosis of breast lesions [15, 16]. AI
210 significantly improves the diagnostic accuracy of doctors and improves the consistency
211 among observers [7]. According to a study of BI-RADS 3 lesions, the computer-aided
212 diagnosis system could correctly upgrade most malignant tumours misdiagnosed as
213 Category 3 by doctors [12]. For Category 4A, AI also exhibited high diagnostic
214 efficiency, and the classification accuracy of BI-RADS 4A can be greater than 0.9 [10,
215 14, 17].

216 Morphological and texture features are the main factors for AI diagnosis.
217 According to the literatures, the use of morphological features and texture features is
218 not limited to the diagnosis of benign and malignant diseases, and these features also
219 help classify malignant tumour subtypes [13, 15, 17-19]. Entropy reflects the
220 complexity and heterogeneous character of lesion texture. Larger entropy indicates
221 more information contained in an image and greater uniformity of the pixel matrix of
222 the image [20]. Compared to benign tumours, the internal components of malignant
223 tumours are more complex. The different proportions of fibrous components,
224 haemorrhage, necrosis, and calcification, result in a heterogeneous echo of malignant
225 tumour. The increase in scattering media causes variation in backscattering, which
226 reduces entropy. Therefore, compared with benign tumours, the entropy of malignant

227 tumours is often reduced [20, 21]. Category 4A benign and malignant lesions are
228 atypical benign and malignant lesions. Our study demonstrated that these atypical
229 benign and malignant lesions were still consistent with previous studies [20, 21]. These
230 findings suggest that careful observation of the internal echo of the lesions will help
231 doctors improve the accuracy of naked eye diagnosis of difficult differentiations
232 between benign and malignant tumours.

233 Category 4A benign and malignant lesions exhibited a significant difference in
234 the number of margin lobulations. The biological behavior of the tumour determines
235 the ultrasonic characteristics. The growth of cancer cells is not uniform and results in an
236 irregular tumour morphology, which is lobulated. On the other hand, the ultrasonic
237 characteristics of the lesions reflect the essential characteristics of the tumour, which is
238 the basis for differentiating between benign and malignant lesions. Therefore, the
239 characteristics of tumour margin are significant in the differentiation of atypical benign
240 and malignant lesions, which is consistent with the literature [11].

241 Calcification can occur in both benign and malignant breast lesions. Most of the
242 calcifications are benign, but a small portion is malignant [22]. Some benign tumours
243 may have mucinous degeneration or hyaline degeneration with dystrophic calcification,
244 which is occasionally difficult to distinguish from breast cancer calcification [23].
245 More calcifications were found in benign lesions in our research, which is consistent
246 with early literatures [22, 24]. These characteristics increase the pathological
247 uncertainty of benign lesions and make these lesions more atypical.

248 Most of the benign lesions grow in parallel, but atypical benign and malignant
249 lesions may also exhibit unconventional characteristics. In this study, the ALS of
250 benign lesions was larger than that of malignant lesions. In a sense, category 4A benign
251 lesions are more like malignant lesions based on some ultrasound features. Category
252 4A malignant lesions exhibit fewer typical malignant signs, and some of their
253 ultrasound features are more similar to those of benign lesions. These differences
254 reflect the characteristics of category 4A lesions. The boundaries of some
255 characteristics between category 4A benign and malignant lesions are indistinct or even
256 inverted and deviate from the signs of typical benign and malignant lesions [25].
257 Difficulty in the differential diagnosis of the two groups causes the classification of
258 benign lesions to be upgraded, whereas the classification of malignant lesions is
259 downgraded.

260 Our study had some limitations. First, the size of our sample was relatively small.
261 Future studies will include a larger number of cases. Second, in the aspect of
262 intralesional calcification, we only studied the value of the number of calcification in
263 the differential diagnosis of BI-RADS 4A benign and malignant lesions, but the
264 significance of the size and shape of calcification in the differential diagnosis was not
265 clear. Finally, this study was based on manually contoured images for quantitative
266 analyses of ROI, which was different from other studies that focused on lesions that are
267 automatically contoured by AI [26]. The present study did not evaluate the automatic
268 identification efficiency for BI-RADS 4A lesions of our AI diagnosis system, and these
269 aspects will be studied in the future.

270 **Conclusions**

271 AI gives us a lot of inspiration. First of all, AI can find out the difference between
272 benign and malignant lesions of BI-RADS 4A, which exceeds the recognition ability of
273 human eyes. Secondly, AI reminds us we should carefully observe whether the lesions
274 are more lobulated and whether the internal echo is more heterogeneous. Especially,
275 the combination of the two features has higher diagnostic value. However, it need a
276 large quantity of cases to determine the threshold of margin lobulation, entropy and
277 internal calcification to diagnose malignant lesions of BI-RADS 4A, our cases are far
278 from enough, especially for the malignant lesions. In the future, we will collect more
279 lesions of BI-RADS 4A and summarize their characteristics so as to obtain a more
280 accurate differential diagnosis threshold.

281

282 **Abbreviations**

283 BI-RADS: Breast Imaging Reporting and Data system; AI: Artificial intelligence; ROI:
284 Region of interest; ALS: Angle between the long axis of the lesion and skin; Cir:
285 Circularity; HWR: Height-to-width ratio; MS: Margin spicules; MC: Margin
286 coarseness; MI: Margin indistinctness; ML: margin lobulation; E: Energy; ENT:
287 Entropy; GM: Grey mean

288 **Ethics approval and consent to participate**

289 This study was approved by the ethics committees of Peking University People's
290 Hospital, Southeast University Zhongda Hospital, the First Affiliated Hospital of
291 Guangxi University of Chinese Medicine and Zhengzhou University First Affiliated

292 Hospital. The four hospitals all granted permission to access and use the medical
293 records described in our study. Written informed consents were obtained from all
294 participants.

295 **Consent for publication**

296 Not applicable.

297 **Availability of data and materials**

298 The datasets used and/or analysed during the current study are available from the
299 corresponding author on reasonable request.

300 **Competing interests**

301 The authors declare that they have no competing interests.

302 **Funding**

303 This work was supported by Beijing Municipal Science & Technology Commission
304 (grant numbers Z181100001918006, 2018). The funder provided support to AI
305 software development and paid the fee for manually contouring.

306 **Authors' contributions**

307 JAZ participated in conceiving and designing the study. SHN drafted the manuscript.
308 JHH, YX1 [Yi Xiao] and MYG developed the Breast ultrasound intelligent diagnosis
309 system and analysed the images using AI. JL, XLL, DW, RFZ, YYW, HMS, MQ, HYL,
310 SHN and XW examined and collected the images of all the patients. DCL, FFL, XMW,
311 YX2 [Yu Xiong] and SQG contoured all the lesions. SHN and XW performed the
312 classifications of all the lesions according to the ACR BI-RADS® Atlas Fifth Edition.
313 All authors have read and approved the manuscript.

314 **Acknowledgments**

315 Not applicable.

316

317 **References**

318 1. Mendelson EB, Böhm-Vélez M, Berg WA, et al. ACR BI-RADS® Ultrasound. ACR
319 BI-RADS® Atlas, Breast Imaging Reporting and Data System. Reston: American
320 College of Radiology, 2013.

321 2. Sadoughi F, Kazemy Z, Hamedan F, Owji L, Rahmanikati M, Azadboni TT.
322 Artificial intelligence methods for the diagnosis of breast cancer by image processing: a
323 review. Breast Cancer (Dove Med Press). 2018; 10: 219-30.

324 3. Bi WL, Hosny A, Schabath MB, Giger ML, Birkbak NJ, Mehrtash A. Artificial
325 intelligence in cancer imaging: Clinical challenges and applications. CA Cancer J Clin.
326 2019; 69(2): 127–57.

327 4. Moon WK, Chen IL, Chang JM, Shin SU, Lo CM, Chang RF. The adaptive
328 computer-aided diagnosis system based on tumor sizes for the classification of breast
329 tumors detected at screening ultrasound. Ultrasonics. 2017; 76: 70-7.

330 5. Becker AS, Mueller M, Stoffel E, Marcon M, Ghafoor S, Boss A. Classification of
331 breast cancer in ultrasound imaging using a generic deep learning analysis software: a
332 pilot study. Br J Radiol. 2018; 91(1083): 20170576.

333 6. Shen WC, Chang RF, Moon WK. Computer aided classification system for breast
334 ultrasound based on Breast Imaging Reporting and Data System (BI-RADS).
335 Ultrasound Med Biol. 2007; 33(11): 1688-98.

- 336 7. Rodr í guez-Cristerna A, G ó mez-Flores W, de Albuquerque Pereira WC. A
337 computer-aided diagnosis system for breast ultrasound based on weighted BI-RADS
338 classes. *Comput Methods Programs Biomed.* 2018; 153: 33-40.
- 339 8. Jamshidii N, Chang J, Mock K, Nguyen B, Dauphine C, Kuo MD. Evaluation of the
340 predictive ability of ultrasound-based assessment of breast cancer using
341 BI-RADS natural language reporting against commercial transcriptome-based
342 tests. *PLoS One.* 2020; 15(1): e0226634.
- 343 9. Ciritsis A, Rossi C, Eberhard M, Marcon M, Becker AS, Boss A. Automatic
344 classification of ultrasound breast lesions using a deep convolutional neural network
345 mimicking human decision-making. *Eur Radiol.* 2019; 29(10): 5458-68.
- 346 10. Huang Y, Han L, Dou H, Luo H, Yuan Z, Liu Q, et al. Two-stage CNNs for
347 computerized BI-RADS categorization in breast ultrasound images. *Biomed Eng*
348 *Online.* 2019; 18(1): 8.
- 349 11. Shan J, Alam SK, Garra B, Zhang Y, Ahmed T. Computer-Aided Diagnosis for
350 Breast Ultrasound Using Computerized BI-RADS Features and Machine Learning
351 Methods. *Ultrasound Med Biol.* 2016; 42(4): 980-8.
- 352 12. Moon WK, Lo CM, Chang JM, Huang CS, Chen JH, Chang RF. Quantitative
353 ultrasound analysis for classification of BI-RADS category 3 breast masses. *J Digit*
354 *Imaging.* 2013; 26(6): 1091-8.
- 355 13. Wu T, Sultan LR, Tian J, Cary TW, Sehgal CM. Machine learning for diagnostic
356 ultrasound of triple-negative breast cancer. *Breast Cancer Res Treat.* 2019; 173(2):
357 365-73.

- 358 14. Lee SE, Han K, Kwak JY, Lee E, Kim EK. Radiomics of US texture features in
359 differential diagnosis between triple-negative breast cancer and fibroadenoma. *Sci Rep.*
360 2018; 8(1): 13546.
- 361 15. Venkatesh SS, Levenback BJ, Sultan LR, Bouzghar G, Sehgal CM. Going beyond a
362 First Reader: A Machine Learning Methodology for Optimizing Cost and Performance
363 in Breast Ultrasound Diagnosis. *Ultrasound Med Biol.* 2015; 41(12): 3148-62.
- 364 16. Le EPV, Wang Y, Huang Y, Hickman S, Gilbert FJ. Artificial intelligence in breast
365 imaging. *Clin Radiol.* 2019; 74(5): 357-66.
- 366 17. Kim K, Song MK, Kim EK, Yoon JH. Clinical application of S-Detect to breast
367 masses on ultrasonography: a study evaluating the diagnostic performance and
368 agreement with a dedicated breast radiologist. *Ultrasonography* 2017; 36: 3-9.
- 369 18. Zhang L, Li J, Xiao Y, Cui H, Du G, Wang Y, et al. Identifying ultrasound and
370 clinical features of breast cancer molecular subtypes by ensemble decision. *Sci Rep.*
371 2015; 5: 11085.
- 372 19. Klimonda Z, Karwat P, Dobruch-Sobczak K, Piotrkowska-Wróblewska H,
373 Litniewski J. Breast-lesions characterization using Quantitative Ultrasound features of
374 peritumoral tissue. *Sci Rep.* 2019; 9(1): 7963.
- 375 20. Tsui PH, Chen CK, Kuo WH, Chang KJ, Fang J, Ma HY, et al. Small-window
376 parametric imaging based on information entropy for ultrasound tissue characterization.
377 *Sci Rep.* 2017; 7: 41004.
- 378 21. Marcon M, Ciritsis A, Rossi C, Becker AS, Berger N, Wurnig MC, et al. Diagnostic
379 performance of machine learning applied to texture analysis-derived features for breast

380 lesion characterisation at automated breast ultrasound: a pilot study. *Eur Radiol Exp.*
381 2019; 3(1): 44.

382 22. Baldwin P. Breast calcification imaging. *Radiol Technol.* 2013; 84(4): 383M-404M;
383 quiz 405M-408M.

384 23. Stöblen F, Landt S, Ishaq R, Stelkens-Gebhardt R, Rezai M, Skaane P, et al.
385 High-frequency breast ultrasound for the detection of microcalcifications and
386 associated masses in BI-RADS 4a patients. *Anticancer Res.* 2011; 31(8): 2575-81.

387 24. Hsu W, Zhou X, Petruse A, Chau N, Lee-Felker S, Hoyt A, et al. Role of Clinical
388 and Imaging Risk Factors in Predicting Breast Cancer Diagnosis Among BI-RADS 4
389 Cases. *Clin Breast Cancer.* 2019; 19(1): e142-51.

390 25. Elverici E, Barça AN, Aktaş H, Özsoy A, Zengin B, Çavuşoğlu M, et al.
391 Nonpalpable BI-RADS 4 breast lesions: sonographic findings and pathology
392 correlation. *Diagn Interv Radiol.* 2015; 21(3): 189-94.

393 26. Zhao C, Xiao M, Jiang Y, Liu H, Wang M, Wang H, et al. Feasibility of
394 computer-assisted diagnosis for breast ultrasound: the results of the diagnostic
395 performance of S-detect from a single center in China. *Cancer Manag Res.* 2019; 11:
396 921-30.

397

398

399

400

401

402 Figure Legends

403

404 Figure 1. Intraductal carcinoma in situ classified as BI-RADS 4A. **a** Ultrasound
405 revealed a solid hypoechoic mass with lobulation. **b** Image contoured manually.

406

407 Figure 2. Adenosis classified as BI-RADS 4A. **a** Ultrasound revealed a solid irregular
408 hypoechoic mass. **b** Image contoured manually.

Figures

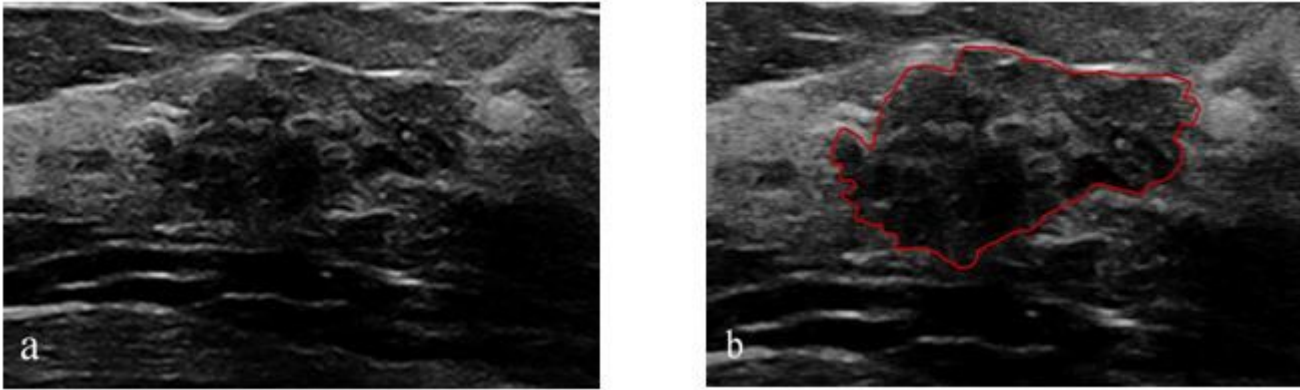


Figure 1

Intraductal carcinoma in situ classified as BI-RADS 4A. a Ultrasound revealed a solid hypoechoic mass with lobulation. b Image contoured manually.

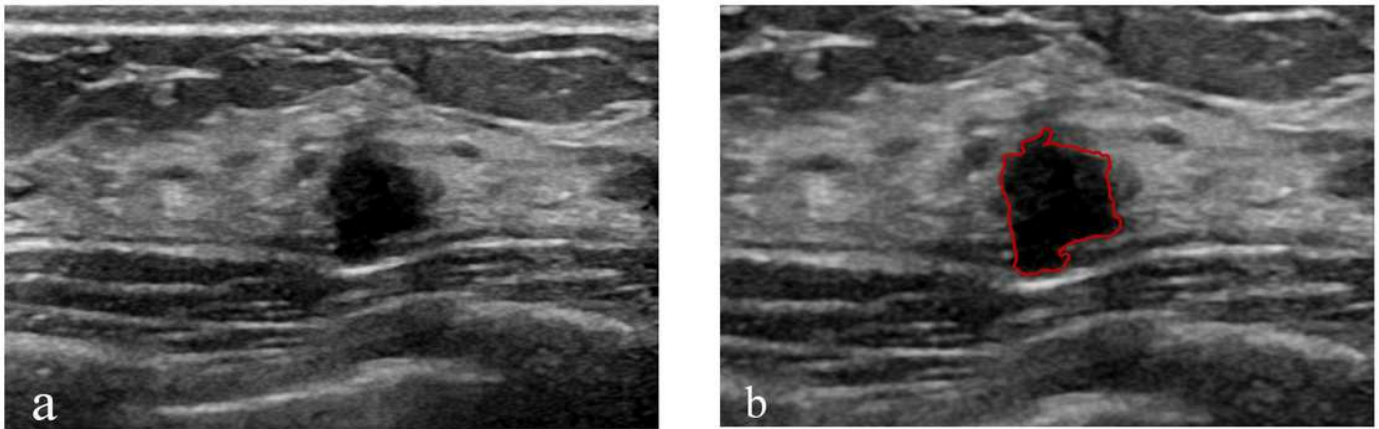


Figure 2

Adenosis classified as BI-RADS 4A. a Ultrasound revealed a solid irregular hypoechoic mass. b Image contoured manually.